Journal of Solar Energy Research (JSER)

Journal homepage: www.jser.ut.ac.ir

The Effect of Sic Polytype on The Solar Cell Characteristics: A Simulation Study

Rand Kareem Husein, Burak Yahya Kadem*

College of Science, Al-Karkh University of Science, Baghdad, Iraq

ARTICLE INFO

Article Type:

Research Article

Received:2026.01.29
Accepted in revised form:2026.05.12

Keywords:
Hybrid solar cell; 3C-SiC; Energy band alignment Interfacial layer; SiC polytypes; Organic-inorganic; heterojunction

A B S T R A C T

Solar cells based on P3HT, SiC, and ZnS were examined via SCAPS-1D to estimate the impact of different silicon carbide (SiC) polytypes as an interlayer, including 3C-SiC, 4H-SiC, and 6H-SiC, on device performance. Different analyses were conducted to explain charge transport and interfacial behavior, including current-voltage (J-V), external quantum efficiency (EQE), Mott-Schottky, and recombination rate. Among the studied solar cells, using 3C-SiC interlayer exhibited the highest performance and a clear reduction in interfacial recombination, achieving a short-circuit current density (J_{SC}) of 15.18 mA/cm², a fill factor (FF) of 81.6%, and a power conversion efficiency (PCE) of 19.2%. Conversely, 6H-SiC has resulted in moderate improvements, whereas 4H-SiC led to a decline in performance. Further optimization of the 3C-SiC interlayer thickness, particularly in the 70-100 nm range, proved critical in balancing band bending, interfacial passivation, and carrier extraction, factors that collectively contributed to maximizing both FF and PCE. Further examinations were carried out to study the effects of trap density, effective density of states, series and shunt resistances, and illumination conditions to evaluate their significance on the solar cell performance. These findings demonstrate that appropriate SiC polytype with careful interface engineering, plays an essential role in enhancing the efficiency of solar cells.

1. Introduction

Silicon carbide (SiC) is a Group IV-IV compound semiconductor made up of silicon and carbon atoms bonded together in a tetrahedral arrangement. These bonds form closely packed atomic layers, and different stacking sequences of these layers give rise to a variety of distinct crystal structures known as polytypes [1]. SiC has become one of the most promising materials for next-generation electronic and optoelectronic devices due to its excellent physical, mechanical, and electronic properties [2,3]. Among the different SiC polytypes, 3C-SiC is mostly attractive due to its promising properties, including a narrow band gap, high electron mobility and drift velocity, and a significantly lower interface trap

*Corresponding Author Email:drburakkadem@gmail.com

Cite this article: Husein, R. Kareem and Kadem, B. Yahya (2026). The effect of SiC polytype on the solar cell characteristics: a simulation study. Journal of Solar Energy Research, 11(2), 2977-2991. doi: 10.22059/jser.2026.410248.1710

DOI: 10.22059/jser.2026.410248.1710

density compared with other SiC polytypes [4,5]. The 3C-SiC polytype has a zinc blende crystal structure and the highest symmetry among all forms of SiC. Because it has a relatively small band gap and does not show spontaneous polarization effects, 3C-SiC is considered very promising for future electronic devices. Interest in this material is increasing due to its wide range of applications, including biosensing, photovoltaics, and solar-driven water-splitting technologies [6-9]. Fig.1A shows the stacking arrangements of the 3C-SiC, 4H-SiC, and 6H-SiC polytypes. In 3C-SiC, the stacking sequence follows a straight, unrotated alignment, while the hexagonal 4H-SiC and 6H-SiC polytypes show zigzag patterns due to alternating layer orientations. In 4H-SiC, the (A) position corresponds to a cubic site and the (B) position to a hexagonal site, while in 6H-SiC, the (A) position is hexagonal and the (B) and (C) positions are cubic. To date, over 200 SiC polytypes have been identified, some exhibiting stacking sequences extending over several hundred bilayers [10]. The physical and electronic properties of SiC are strongly influenced by both the polytype structure and the local atomic environment within each stacking configuration. Among the three SiC polytypes, 3C-SiC, having a single terrace [11, 12], possesses a simpler, more uniform surface, which may lead to lower defect density and better interfacial uniformity when used in heterojunctions or thin-film devices.

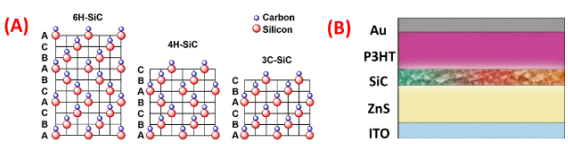

Figure 1. (A) SiC polytypes [13] and (B) solar cell architecture with SiC interlayer

Janz and co-authors [14] have shown that SiC is the most promising interlayer in crystalline silicon thin-film solar cells because its electrical behavior can be effectively modified by doping with boron or phosphorus. Also, Sameera and co-authors [15] have proposed 3C-SiC as a non-toxic alternative buffer layer for p-CdTe/n-3C-SiC/n-SnO_2 heterojunction solar cells. They simulated the effects of 3C-SiC thickness, doping concentration, and defect density to optimize solar cell performance using SCAPS-1D simulations. Recently, Zouache and co-authors [16] highlighted 3C-SiC as a promising buffer-layer material for advancing the efficiency of next-generation CIGS thin-film photovoltaics. They demonstrated an optimized design with excellent performance, including an efficiency of 32.83%, V_{OC} of 0.86 V, J_{SC} of 56.40 mA/cm², and FF of 80.79%. Although SiC is costlier than silicon, its application in solar cells can be economically justified when long-term performance is considered. SiC offers a significantly longer operational lifetime [17], which may reduce maintenance costs compared to silicon. In addition, its superior durability and lower degradation rate enhance overall energy yield over time, which can help offset the higher initial material cost. Conventional Si solar cells typically exhibit degradation rates of ~0.8% per year due to mechanisms such as light-induced degradation, thermal stress, and environmental effects [18]. In contrast, SiC, owing to its wide bandgap and strong bonding [17], is much less susceptible to these degradation pathways, with expected rates below ~0.2% per year, particularly under harsh conditions. However, long-term field data for SiC-based solar cells are still limited, and further validation is required. These properties suggest strong potential for reliable operation in real-world environments. However, we agree that experimental validation is essential to fully confirm the practical applicability of the proposed design. In the current study, different SiC polytypes were used as efficient interlayers in P3HT/ZnS hybrid solar cells. The authors believe that this study provides more detailed insight into the effect of the SiC layer in hybrid solar cell applications. However, the long-term stability of a ZnS/SiC/P3HT solar cell is a critical concern, particularly under heat and humidity. The organic component (P3HT) is known to be more vulnerable to thermal and moisture-induced degradation, which can impact device performance over time. The SCAPS simulations were performed under idealized and stable material conditions to evaluate the intrinsic potential of the proposed device. Therefore, degradation effects related to environmental stress were not explicitly considered, which may lead to an optimistic estimation of stability.

2. Device Model and Simulation Parameters

In this study, the effect of inserting SiC polytypes between P3HT and ZnS layers was simulated using 1D-SCAPS software; see Fig.1B for the device architecture. The solar cells were simulated under AM 1.5 G 1 sun and 100 mW/cm^2 illumination, where Zinc sulfide (ZnS) was used as an n-type semiconductor and electron transport layer (ETL).

Poly(3-hexylthiophene) (P3HT) as the hole transport layer (HTL) and organic absorber layer. The polytypes of silicon carbide (SiC) are used as intrinsic

layers. To obtain the current density-voltage (J-V) characteristics, SCAPS 1D software uses the following Poisson, continuity, and carrier transport equations [19]:

$$\Delta\varepsilon\Delta\phi = = q(p - n + N_D^+ - N_A^-) \quad (1)$$

For electrons:

$$\Delta J_n = q(R - G) + q\frac{\partial n}{\partial t} \quad (2)$$

For holes:

$$\Delta J_p = q(R - G) + q\frac{\partial p}{\partial t} \quad (3)$$

For electrons:

$$J_n = D_n\frac{dn}{dx} + \mu_n n\frac{d\phi}{dx} \quad (4)$$

For holes:

$$J_p = D_p\frac{dp}{dx} + \mu_p p\frac{d\phi}{dx} \quad (5)$$

where ε is the dielectric constant; N_D and N_A are the donor and acceptor densities, respectively; p and n are the free holes and free electrons; ϕ is the electrostatic potential; J_n and J_p are the current densities for the electrons and the holes, respectively; R and G are the recombination and generation rates, respectively; and μ_n and μ_p are the electron and hole mobility, respectively. These solar cells were simulated based on the materials' properties illustrated in Table 1. Also, Fig.2 shows the methodology steps for this study.

Table 1. The parameters used in the SCAPS-1D software to simulate and evaluate the solar cell performance

Parameter	ZnS [20]	3C-SiC [16]	4H-SiC [21]	6H-SiC [21]	P3HT [17]
d (μm)	100nm	100nm	100nm	100nm	100nm
χ (eV)	4.5	3.8	3.1	3.3	1.7
E_g (eV)	3.7	2.36	3.26	3.02	3.5
ε_r	9	9.72	9.76	9.66	3
DOS_{CB} (Nc) (cm^{-3})	2.2×10^{18}	1.5×10^{19}	1.8×10^{19}	8.8×10^{19}	2.2×10^{18}
DOS_{VB} (Nv) (cm^{-3})	1.8×10^{19}	1.9×10^{19}	2.1×10^{19}	2.2×10^{19}	2.2×10^{18}
μ_e ($cm^2 V^{-1} s^{-1}$)	100	900	950	420	$1.8x10^{-3}$
μ_h ($cm^2 V^{-1} s^{-1}$)	25	3	3	6	$1.8x10^{-2}$
N_D (cm^{-3})	1×10^{18}	5×10^{15}	8.21×10^{-9}	1.85×10^{-8}	0
N_A (cm^{-3})	0	5×10^{15}	8.21×10^{-9}	1.85×10^{-8}	1×10^{18}

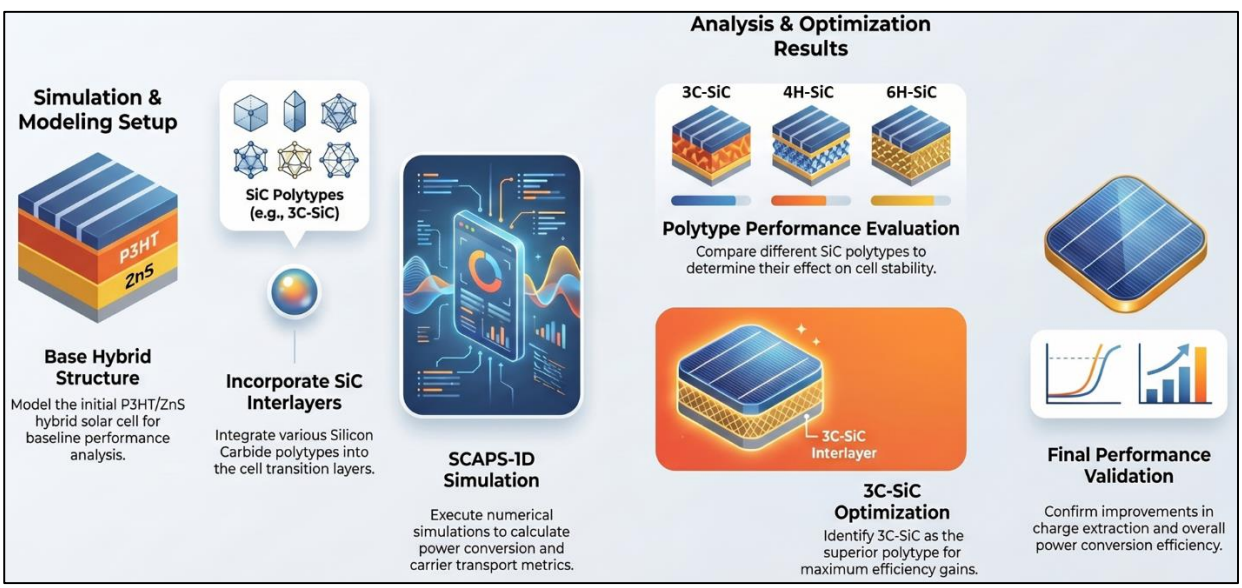

Figure 2. the methodology flow chart (this image is created by the assistance of ***Google Notebook***)

3. Results and discussions

3.1. J-V characteristics

The current-voltage (J-V) characteristics of the hybrid solar cells (see Fig.3A) based on the P3HT/SiC/ZnS heterojunction reveal distinct performance variations depending on the SiC polytypes, including 3C-SiC (cubic), 4H-SiC (hexagonal), and 6H-SiC (hexagonal), and exhibit different electrical behaviors owing to their structural and electronic properties. The photocurrent was simulated under AM1.5G solar illumination with an intensity of 100 mW/cm². The fill factor (FF) and power conversion efficiency (PCE) of the studied solar cells were determined using the following relations [22]:

$$PCE(\%) = \frac{J_{max}V_{max}}{P_{in}} \quad (6)$$

$$FF = \frac{J_{max}V_{max}}{J_{sc}V_{oc}} \quad (7)$$

where J_{SC} is the short-circuit current density (mA/cm²), V_{OC} is the open-circuit voltage (V), P_{in} is the incident light power, and J_{max} (mA/cm²) and V_{max} (V) represent the current density and voltage at the maximum power point in the J-V characteristics, respectively. The overall performance of the pure and SiC-based solar cells demonstrates clear variations depending on the SiC polytype incorporated into the device structure. As illustrated in Fig.3B, the reference device exhibits a J_{SC} of 13.76 mA/cm², V_{OC} of 1.54 V, FF of 66.1%, and PCE of 14.0%. Adding a 3C-SiC interlayer has resulted in a clear improvement in the photovoltaic performance: the J_{SC} increases to 15.18 mA/cm², FF improves to 81.6%, and the PCE reaches 19.2%, while the V_{OC} remains nearly unchanged.

These results suggest more efficient charge extraction and a significant reduction in recombination losses at the interface. On the other hand, adding a 6H-SiC interlayer results in only slight improvements compared to the reference device. Although its J-V characteristics are similar to those of the 3C-SiC-based device, J_{SC} decreases to 12.5 mA/cm². Recombination losses are still noticeable, and PCE remains lower than that achieved by 3C-SiC. Furthermore, using a 4H-SiC interlayer exhibits a clear drop in J_{SC} to 11.64 mA/cm², FF declines sharply to 20.74%, and PCE is significantly reduced to 4.6%, even though V_{OC} remains relatively high at 1.9 Volt. The latter results are likely attributed to increased series resistance and interfacial energy barriers, as indicated by the S-shaped J-V curve (Fig.1A), and suggest inefficient carrier transport and increasing recombination losses, which lead to hindered charge transport, lower the FF and reduce the J_{SC} [23,24]. The differences in solar cell performance between the SiC polytypes can be explained by their different stacking arrangements, which affect carrier mobility and the distribution of the internal electric field at the heterojunction. These results show that selecting the appropriate SiC polytype is crucial for controlling charge transport and interfacial behavior in hybrid heterojunction solar cells [25]. To better understand these performance differences, additional electrical and optoelectronic characterizations were carried out, including external quantum efficiency (EQE) measurements. As shown in Fig.3C, the EQE results confirm the higher J_{SC} observed for the device with the 3C-SiC layer. This is expected because J_{SC} is directly related to EQE due to the following equation [26]:

$$J_{ph} = J_{SC} = e \int EQE\, \Phi_{AM1.5g}(E)\, dE \quad (8)$$

where e is the elementary charge, $\Phi_{AM1.5g}(E)$ is the photon flux, and (E)dE is the photon energy (or wavelengths) to produce the photocurrent density J_{ph}, which is, at the short circuit condition, equal to the J_{SC}.

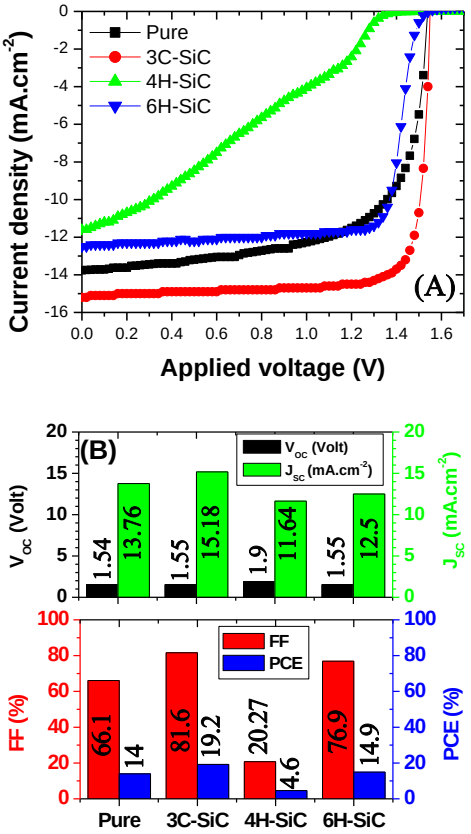

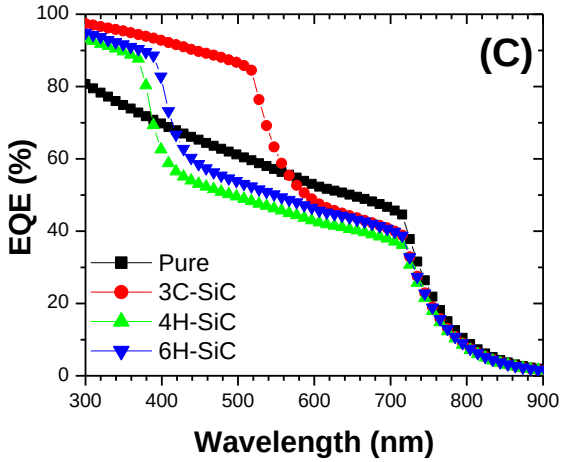

Figure 3. (A) I-V (B) solar cell parameters, and (C) EQE spectra for the solar cells with different SiC

The EQE spectra show different behavior based on the SiC polytype. The 3C-SiC-based solar cell reveals the highest EQE response within the visible wavelength range (~400-550 nm), which is in good agreement with their high J_{SC}. This enhanced EQE is mainly attributed to the smaller band gap of 3C-SiC [25], which enables higher absorption of visible light as well as the efficient charge collection at the interfaces. On the other hand, a 4H-SiC-based device shows the lowest EQE across the visible range. This weak response is reliable with the wider band gap of 4H-SiC (3.26 eV) [25], which shifts absorption toward shorter wavelengths. As a result, these devices absorb fewer photons and may experience higher interfacial recombination, aligning with their lower J_{SC} and PCE. Solar cells based on 6H-SiC show an EQE response between those of 3C-SiC and 4H-SiC. This moderate performance is attributed to the indirect nature of the 6H-SiC band gap (3.05 eV) [25] and relatively lower carrier mobility, both of which limit photon absorption and hinder charge extraction efficiency compared to the 3C-SiC-based devices. In general, EQE results verify the J-V characteristics, confirming that 3C-SiC delivers the most efficient photocarrier generation and extraction compared to other SiC polytypes. This is attributed to improved interfacial band alignment and defect passivation. SiC interlayers are known to suppress defect-assisted recombination and enhance electron extraction in thin-film heterojunctions. Previous studies on SiC-based buffer layers in CdTe, CIGS, and Sb_2 Se_3 solar cells consistently report reduced interface recombination and improvements in J_{SC} and FF [15]. In this work, we show for the first time that the performance of P3HT:ZnS hybrid solar cells is highly dependent on the SiC polytype, driven by variations in band gap, carrier transport, and interfacial recombination characteristics. The improved EQE after using a 3C-SiC interlayer suggests more efficient carrier collection, prompting further analysis of charge transport and recombination processes.

3.2. Mott-Schottky analysis and recombination rate

Further investigations were carried out using Mott-Schottky analysis ($1/C^2$ vs. applied voltage) based on C-V measurement (see Fig.4A) to study the effect of inserting different polytypes of SiC as an interlayer between P3HT and ZnS and their influences on the junction behavior of hybrid organic-inorganic solar cells. In the pure device, where there is no SiC interlayer, the steep slope of the $1/C^2$-V plot and the lower voltage intercept indicate a low built-in potential (V_{bi}) and a high effective acceptor concentration (N_A) according to the following equation [27]:

$$N_A(W) = \frac{2}{q\varepsilon_r\varepsilon_0}\left(\frac{1}{A^2}\frac{d(1/C^2)}{dV}\right) \quad (9)$$

where W is the depletion width, A is the junction area, ε_r is the semiconductor relative permittivity, $\varepsilon_0$is the vacuum permittivity, q is the electronic charge, and $\{d(1/C^2)/dv\}$ is the slope of Fig.4A.

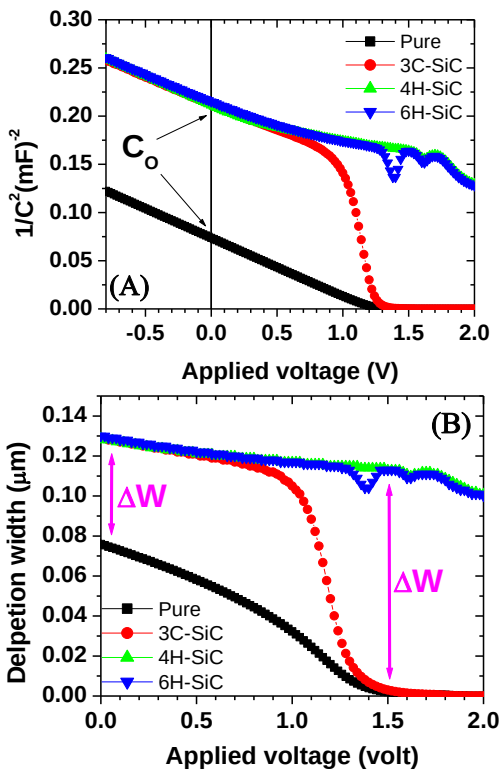

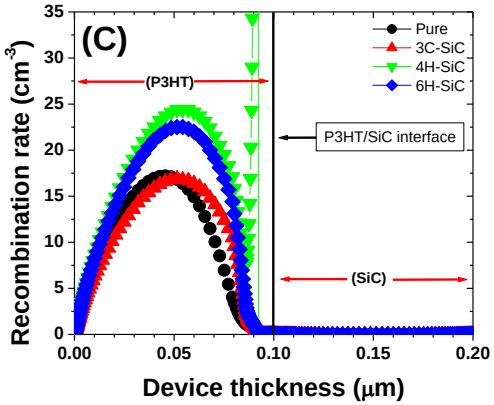

Figure 4. (A) $1/C^2$ vs. applied voltage, (B) Depletion width vs. applied voltage, and (C) Recombination rate vs. device thickness for the solar cells under study based on different SiC

The doping profiles calculated using equation 9 are typically a function of the depletion width, which is determined from the measured capacitance using [27]:

$$W(V) = \frac{\varepsilon_r \varepsilon_0 A}{C(V)} \quad (10)$$

Since both W and C vary with voltage, this approach assumes uniform material properties across the depletion region. However, in the present case, the device is a heterostructure, meaning that the depletion region may extend across the intrinsic region, as shown in Fig.4B.The insertion of an i-layer usually has a great impact on the PN junction devices [28]. The capacitance of the PN device has increased and exhibited higher depleted behavior after adding a SiC layer [29] as demonstrated in Fig.4A. This suggests a less efficient depletion region and suboptimal band alignment at the P3HT/ZnS interface. The slope becomes shallower upon inserting 3C-SiC, and the intercept shifts to a higher voltage (~1.25 V). This indicates a lower N_A, a stronger V_{bi}, and an improved depletion region. This is attributed to the non-polar, zinc-blende structure of 3C-SiC, which enables better interface uniformity and fewer trap states. In contrast, devices incorporating the hexagonal polytypes (4H-SiC and 6H-SiC) show further increases in nominal V_{bi} but poorer linearity and oscillations in their $1/C^2$-V plots. This behavior results from inherent polarization effects and fixed charges associated with hexagonal SiC polytypes, which partially screen the junction field and degrade the ideal depletion behavior. Therefore, while all SiC interlayers improve the junction relative to the pure device, 3C-SiC yields the most favourable behavior. These findings are consistent with prior reports of improved electronic behavior in 3C-SiC heterojunctions (e.g., for charge separation in solar-driven devices) [30]. To interpret these electrical characteristics, the energy band alignment and carrier transport mechanisms were further analysed.

3.3. Interface properties

The recombination rate is evaluated based on using different SiC polytypes as an interlayer in a P3HT/ZnS-based hybrid solar cell, as shown in Fig.4C. The insertion of SiC considerably affects interfacial recombination compared to the pure device, confirming that the SiC interlayer effectively passivates interface traps and improves charge separation at the P3HT/ZnS interface. Among the examined polytypes, the 3C-SiC interlayer shows the lowest recombination rate, followed by 6H-SiC, whereas 4H-SiC exhibits the highest recombination among the SiC-modified devices. This behavior is due to differences in band alignment and defect properties among the SiC polytypes (see Fig.5). The narrower band gap (~2.36 eV) and higher electron affinity of 3C-SiC provide better energy alignment at the P3HT/SiC/ZnS junction, allowing electrons to move more easily and reducing recombination (Fig. 5B). In contrast, 4H-SiC and 6H-SiC have wider band gaps and larger band offsets, which block electron transport and increase recombination losses (Fig.5C and Fig.5D). Charge transport in solar cells is different between organic and inorganic semiconductors. In organic semiconductors, charge transport is generally governed by a hopping mechanism, where charge carriers move between localized states. This performance arises from the presence of disorder and structural imperfections in organic materials. In contrast, inorganic semiconductors typically exhibited more ordered crystal structures, enabling band-like transport, where charge carriers move freely through the conduction and valence bands [31]. The movement of electrons in the conduction band and holes in the valence band under an external electric field results in conductivity. Upon absorption, P3HT creates an electron-hole pair called an exciton. The latter is dissociated to reach the interface and separated to free electron and hole charge carriers, as holes move in one direction and electrons move oppositely to their respective electrodes [32].

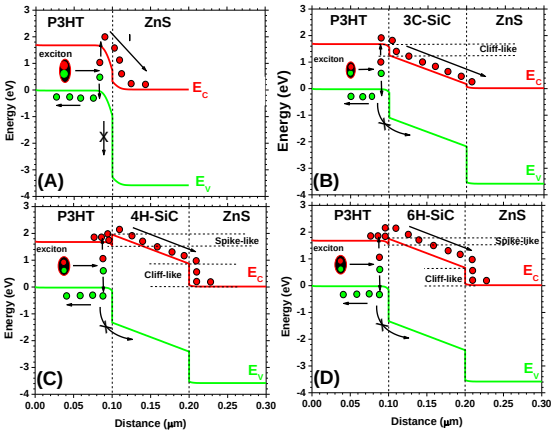

Figure 5. Energy band bending of (A) P3HT/ZnS, (B) P3HT/3C-SiC/ZnS, (C) P3HT/4H-SiC/ZnS, and (D) P3HT/6H-SiC/ZnS

In the pure device, the cliff-like structure at the P3HT/ZnS interface is created (see Fig.5A) and may result in a higher recombination rate at the interface due to the accumulated electrons [33]. Using a 3C-SiC layer has resulted in a wider depletion gradient over the layer thickness (100nm) as shown in Fig.5B. The conduction band offset between P3HT and 3C-SiC shows a cliff-like structure confirmation where the conduction band minimum (CBM) of 3C-SiC is higher than that of the P3HT, which is undesirable because it results in higher recombination paths in the trap states within the band gap [34] (as confirmed by Fig.4C, where the recombination of the 3C-SiC-based device show slightly lower rate and shifted slightly close to the P3HT/SiC interface). However, the higher generation rate, as confirmed by EQE results in Fig.3C, may overcome the recombination rate shown in Fig.3C, resulting in higher J_{SC}. In the case of using 4H- and 6H-SiC, the band alignment exhibited an obvious band-offset spike-like structure confirmation at the P3HT/SiC interface, which directly influences the interface recombination [35]. The spike-like structure in Fig.5C confirms that the CBM of the SiC layer is higher than the P3HT layer by about 0.4eV, and a cliff-like structure of about 0.6eV is created at the SiC/ZnS interface. Such a structure is unfavourable for charge collection, and a higher recombination rate occurred, as confirmed by Fig.4C. It has been reported that in order to achieve the best solar cell performance, conduction band offset needs to be moderately positive (spike-like) [36]. For intrinsic semiconductors, electron and hole concentrations remain in equilibrium at a given temperature. Mostly, the conductivity depends on two factors: the carrier concentrations (n and p), which vary with temperature, and the carriers' mobility, which is determined by their ability to move through the lattice without frequent scattering. Electron-electron scattering is typically negligible at low carrier concentrations [31]. The total current density in the solar cells is therefore determined by [37]:

$$J_{tot} = J_n + J_p = qn\mu_n E + qp\mu_p E \quad (11)$$

$$J_{tot} = qE(n\mu_n + p\mu_p) \quad (12)$$

where (J_{tot}) is the total current density and (E) is the applied electric field. Since current density is also related to conductivity (σ) and electric field (E) by Ohm's law [37]:

$$J_{tot} = \sigma E \quad (13)$$

By comparison with Equation (12), the conductivity is determined based on the mobility according to the following equation [31]:

$$\sigma = q(n\mu_n + p\mu_p) \quad (14)$$

The carrier concentration in an energy band depends on the occupation probability f(E) and the density of states g(E) [31]:

$$n = \int g(E)f(E)dE \quad (15)$$

where f(E) is the Fermi-Dirac function [31, 38]:

$$f(E) = \frac{1}{1+exp(\frac{E-E_F}{k_BT})} \approx exp(-\frac{E-E_F}{k_BT}) \quad (16)$$

which simplifies to the Boltzmann form when $E >> K_BT$, where E_F is the Fermi level energy. The electron concentration in the conduction band is then given by [39]:

$$n = \int_{E_C}^{E_C+\chi} g_{CB}(E)f(E)dE \quad (17)$$

where the density of states functions $g_{CB}(E)$ depends on the semiconductor material [38]. The charge carrier's distribution is shown in Fig.6A for intrinsic, where the Fermi level (E_F) position is at the middle of the band gap; (Fig.6B) for p-type semiconductor, where E_F is shifted towards the valence band; and (Fig.6C) for n-type semiconductor, where E_F is shifted towards the conduction band.

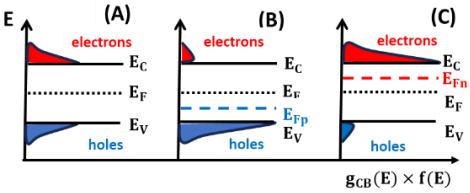

Figure 6. Carriers' distributions and Fermi level at (A) intrinsic semiconductor (Fermi level in the middle of the band gap), (B) P-type semiconductor (Fermi level shifts toward the valence band), and (C) n-type semiconductor (the Fermi level shifts toward the conduction band)

Under constant potential, most conduction-band electrons occupy energy levels near the band edge (E_C) and $\chi >> K_BT$, the integration limits in Equation (17) can be extended from E_C to ∞ [40]. Substituting and integrating yields the electron concentration:

$$n = N_C exp[-\frac{E_C - E_F}{k_B T}] \quad (18)$$

N_C is the effective density of states at the conduction band edge (E_C). Similarly, the hole concentration in the valence band is:

$$p = N_V exp[-\frac{E_F - E_V}{k_B T}] \quad (19)$$

where (N_V) represents the effective density of states at the valence band edge (E_V). Fig.7 presents the simulated carrier concentration densities (electron n and hole p) across the P3HT/ZnS solar cell in the pure structure and with SiC interlayers of different polytypes (3C-, 4H-, and 6H-SiC).

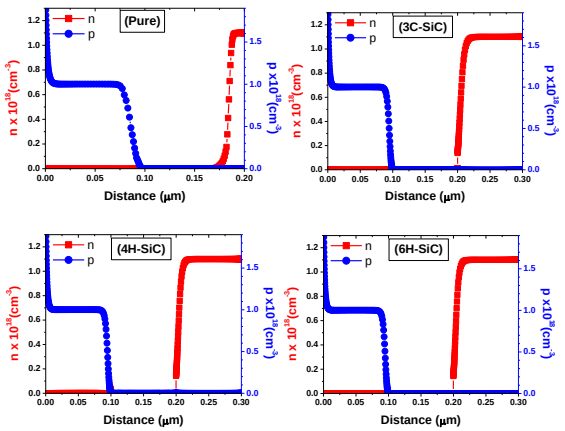

Figure 7. The simulated concentration of these charge carriers with respect to their position in the device.

In the pure P3HT/ZnS device, the carrier distribution exhibits a sharp transition for the p-rich (P3HT) region at the interface, which suggests a higher hole concentration in the P3HT layer. On the other hand, the n-rich (ZnS) region indicates a higher electron concentration starting from the middle of the ZnS layer. Indicating that the space charge region is extended inside the ZnS layer. Upon inserting SiC between P3HT and ZnS, the position and slope of the n/p transition are significantly modified, especially for the electron density of state, demonstrating the sensitivity of the internal electric field and carrier confinement to the electronic properties of the SiC interlayer. These differences arise from changes in the band offsets at the P3HT/SiC and SiC/ZnS interfaces. Since each SiC polytype has a different band gap and electron affinity, the band offsets change accordingly and controls whether electrons or holes can move easily across the interlayer [41]. The SiC interlayer modifies V_{bi} and the space-charge region; as a result, 3C-SiC creates the smallest barrier in the conduction band, allowing electrons to move more easily toward the ZnS layer. In contrast, 4H-SiC and 6H-SiC form larger conduction band barriers, which restricts electron transport, reduces interfacial recombination, and contributes to improvements in both V_{OC} and FF. In contrast, poor band alignment or a thick interfacial barrier increases series resistance and limits current extraction [42], which explains the lower performance of 4H-SiC-based devices. In addition, SiC interfaces can contain fixed charges and trap states that disturb the internal electric field. These traps capture charge carriers, increase recombination, and reduce overall device efficiency, as widely reported in organic and hybrid solar cells [43]. Passivating interface states helps keep a high carrier density near the junction and reduces SRH recombination. Among the SiC polytypes, 3C-SiC provides the best charge balance and the lowest energy barrier, leading to better carrier extraction and device performance. These results confirm that using a thin, well-designed SiC interlayer can improve photovoltaic performance by reducing interface recombination and improving charge selectivity [44]. 3C-SiC is promising because of its favourable conduction-band alignment with ZnS and its ability to block holes from P3HT without introducing excessive resistance. Future optimization focuses on tuning SiC properties.

3.4. Characteristics of 3C-SiC

3.4.1. Different thicknesses

The band offsets at both the P3HT/3C-SiC and 3C-SiC/ZnS interfaces impact the charge-transfer

behavior and are crucial to understanding the thickness-dependent performance trends [45]. Therefore, different thicknesses of the 3C-SiC layer were used to evaluate the effect of the thickness on the solar cell performance. The position of CBM and VBM defines the energetic barriers for electron and hole movement, as well as determines the strength and direction of the internal electric field. Generally, ETL and HTL layers are essential for collecting photo-generated charge carriers in solar cells. When light is absorbed by the absorbing layer, it generates excitons (electron-hole pairs) with low binding energy and relatively long diffusion lengths [46]. As a result, these excitons reach the interface, where they are separated by the electric field associated with the space-charge layer. Once separated, the electrons and holes move toward their respective electrodes and finally flow through the external circuit via the metal contacts [47]. The simulated band diagrams (Fig.8A) for various 3C-SiC thicknesses demonstrate that the SiC interlayer is crucial in creating the internal electric field across the active junction, as demonstrated by the Mott-Schottky curve in Fig.8B, where the higher SiC thickness exhibited a higher gradient. At the P3HT/SiC interface, the conduction- and valence-band offsets generate V_{bi} that promotes efficient exciton dissociation while suppressing interfacial recombination, thereby contributing to a notable improvement in device performance [48]. The higher V_{bi} indicates stronger charge-separation capability [49], while the decreasing slope proposes lower interface trap density and better effective carrier concentration. The trap's states' energetic profile can be extracted from the frequency dependence of the capacitance.

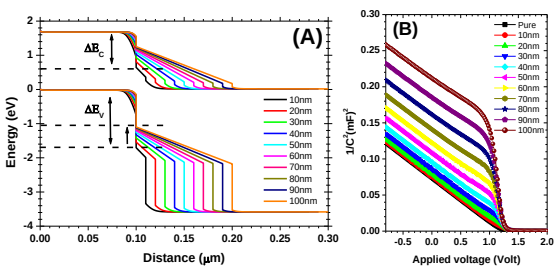

Figure 8. (A) Band alignment and (B) Mott-Schottky curve for the P3HT/3C-SiC/ZnS with different 3C-SiC thicknesses

The trap density of states (t-DOS) at a given energetic level is calculated using the following equation [50]:

$$N_t(E) = -\frac{V_{bi}}{qWkT}\ \frac{dC}{d(ln\,\omega)} \tag{20}$$

where W is the width of the space-charge region, ω ω=2πf is the angular frequency, k is the Boltzmann constant, and T is the measurement temperature. The product kT represents the thermal energy of the carriers interacting with the trap states. This reduction in the trap states is consistent with the smoother band profiles and reduced recombination identified in the simulations. When the 3C-SiC layer is very thin (10-30 nm), the entire potential drop between P3HT and ZnS is confined to a short physical region, resulting in pronounced band bending at both interfaces. These steep discontinuities generate strong internal electric fields that facilitate exciton dissociation by directing electrons toward the ZnS side and holes toward the P3HT side. However, such abrupt band offsets are also linked to intensified interactions with interface traps and increased non-radiative recombination, a behavior frequently reported for ultrathin inorganic interlayers in hybrid heterojunction devices [51]. This explains the lower FF and moderate PCE observed for ultra-thin 3C-SiC layers. Consequently, device performance in this regime remains moderate, with PCE ≈ 15-16% and FF ≈ 70-74% as shown in Fig.9A and Fig.8B. When the thickness of the 3C-SiC layer is increased to 40-60 nm, the conduction and valence bands change more smoothly across the junction (Fig. 8A). This gradual transition spreads V_{bi} over a wider region, reducing sudden energy barriers and trap effects. As a result, charge carriers move more easily, mainly by drift rather than tunnelling [52], which improves charge extraction efficiency. Devices in this thickness range show a higher V_{OC} of about 1.55 V, a slightly higher J_{SC} of ~14.6 mA/cm², and an improved FF of ~78%. This leads to a PCE of around 17.8%,

indicating an optimal balance between strong internal electric fields and reduced recombination losses.

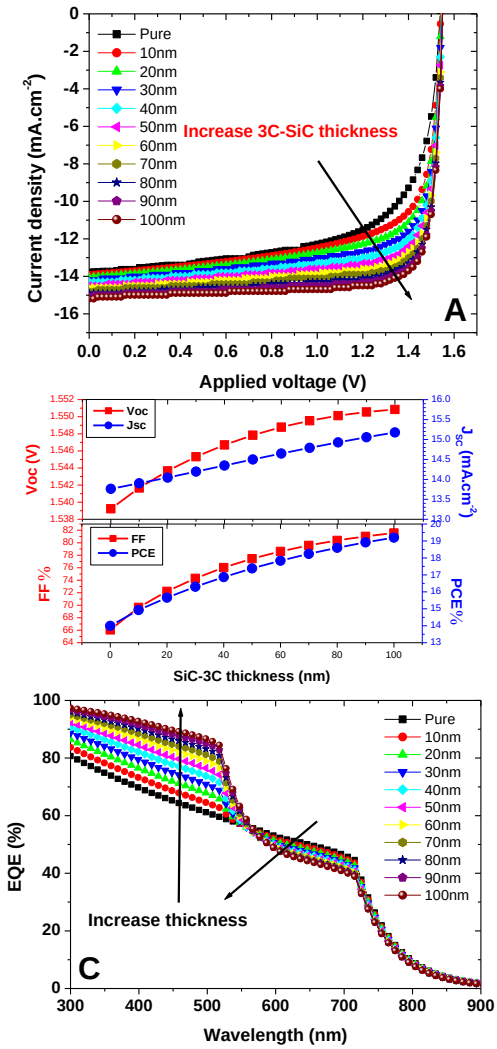

Figure 9. (A) I-V characteristics of solar cells with different 3C-SiC interlayer thicknesses, (B) the photovoltaic parameters as a function of 3C-SiC thickness, and (C) EQE spectra of solar cells with different 3C-SiC interlayer thicknesses

Larger thicknesses (70-100 nm) induce smoother and more extended band bending, indicating effective interfacial passivation and a well-distributed V_{bi}. The steady rise in FF to approximately 81% and in PCE to about 19.2% at 100 nm demonstrates enhanced charge-blocking capability and reduced recombination losses. In addition, the continuous increase in V_{OC} further supports the suppression of non-radiative recombination and improved energy-level alignment at the interfaces. Further enhancement is confirmed by simulating External Quantum Efficiency (EQE) spectra of the P3HT/3C-SiC/ZnS heterojunction solar cell for various 3C-SiC interlayer thicknesses. EQE data presented in Fig.8C display a clear thickness-dependent trend across the visible region. An absorption edge near 700 nm related to the P3HT main absorption spectra is slightly red-shifted compared to experimental observations; usually, P3HT absorption exhibits a shoulder around 650 nm in the pure device, which is associated with interchain stacking transitions [22]. This shift in the simulated spectrum suggests enhanced molecular ordering or increased conjugation length within the P3HT phase in the model. After adding the SiC layer, all devices exhibit a strong response in the visible region (350-550 nm) related to the SiC with a band edge close to 550nm, followed by a slight decrease in the absorption intensity after 550nm toward longer wavelengths due to the limited absorption of P3HT and ZnS near the optical band edge. Increasing the thickness of the 3C-SiC layer raises the EQE intensity in the 400-600 nm range without changing the overall spectral shape, indicating that light absorption remains the same. The improvement instead comes from better charge transport and improved interface quality. The higher EQE matches the increase in J_{SC}, confirming that the 3C-SiC interlayer helps charge extraction by smoothing the interfacial potential and reducing recombination losses [40].

3.4.2. Optimizing different SiC parameters

Several SiC-related parameters were studied to optimize solar cell performance, including the conduction band effective density of states (DOS_{CB}), total trap density (Nt), operating temperature, series resistance (R_S), shunt resistance (R_{Sh}), and incident light intensity. Increasing DOS_{CB} mainly affects the V_{OC}, FF, and PCE, while the J_{SC} remains largely unchanged, as shown in Fig.10A. On the other hand, Nt has a much stronger impact on device performance. Higher Nt values reduce FF and PCE (Fig.10B) because they act as recombination centers through SRH processes, resulting in reducing carrier lifetime and limiting quasi-Fermi level splitting [53]. Typically, increasing the temperature increases carrier energy distribution, raises the intrinsic carrier concentration, and enhances non-radiative recombination and results in lower V_{OC} as shown in Fig.10C [54, 55].

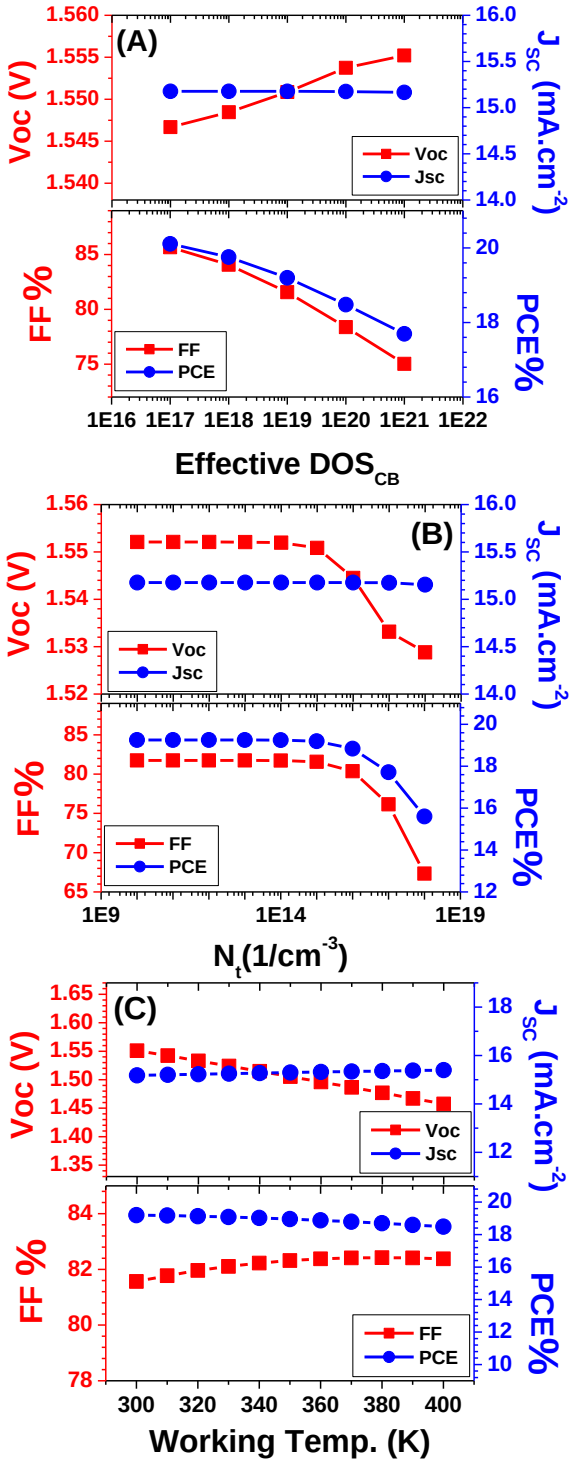

Figure 10. (A) Different effective DOS_{CB} in 3C-SiC, (B) Different Nt in 3C-SiC, and (C) different working temperatures

Shunt resistance (R_{Sh}) controls leakage pathways in the device, where low R_{Sh} values typically reduce V_{OC} and FF. As shown in Fig.11A, increasing R_{Sh} leads to higher FF and PCE, highlighting the role of internal recombination in device performance. In contrast, increasing the series resistance (R_S) causes a gradual decrease in FF due to increased voltage losses along the charge-transport path, as illustrated in Fig.11B, which ultimately lowers the PCE. When R_S is low, the FF remains high and stable, indicating efficient carrier extraction and minimal resistive losses [56]. In this range, both V_{OC} and J_{SC} remain nearly constant. The dependence of solar cell performance on the light intensity is shown in Fig.10C where the J_{SC} is increased with increasing light intensity. Under short-circuit conditions, the dominant recombination process is largely independent of illumination level, and J_{SC} follows a power-law relationship with the incident light intensity [57]:

$$J_{sc} \propto P_{light}^{\alpha} \tag{21}$$

where α is the recombination coefficient, and P denotes the incident optical power. The nearly linear behavior observed in Fig.11C, where α is the slope, is close to 1. Values of α close to unity indicate that photocurrent losses are governed by recombination-limited transport rather than space-charge effects or field-dependent collection [28, 58]. The latter results in low FF, whereas increasing V_{OC} with increasing illumination is observed. It is governed by the following relation [59]:

$$V_{OC} = V_{OC}^{`} + \frac{nkT}{q} ln(X) \tag{22}$$

The term (V'_{OC}) represents the voltage at a reference illumination level (often 1 sun). The term, $\frac{nkT}{q}\ln(X)$, shows how V_{OC} increases logarithmically as the illumination factor (X) increases. Here, (n) is the diode ideality factor.

Table 2. This work compared with other reported solar cells using 3C-SiC interlayer in diffreent solar cells types

Type	Buffer/Abso.	PCE (%)	Ref.
Theor.	3C-SiC/CIGS	25.51	[60]
Theor.	3C-SiC/CdTe	17.29	[15]
Theor.	3C-SiC/P3HT	19.2	This work

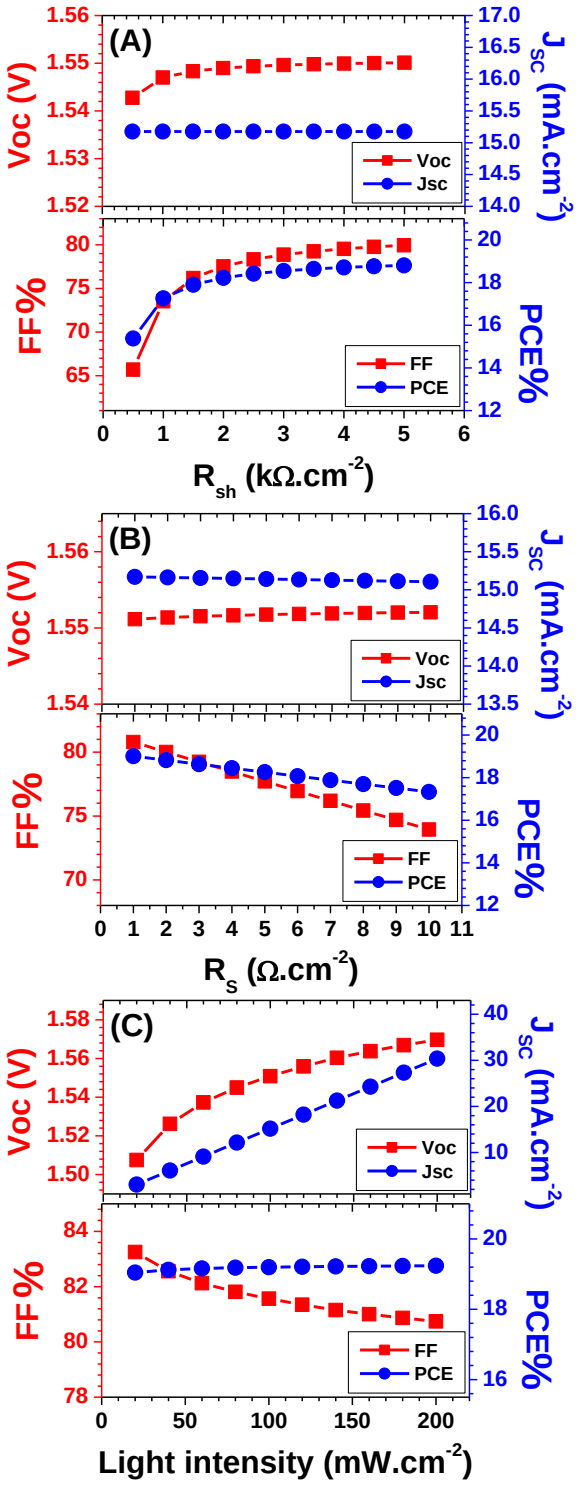

Figure 11. (A) different R_S, (B) different R_{Sh}, and (C) different light intensity

Sameera and co-authors [15] have studied cubic silicon carbide (3C-SiC) as promising non-toxic buffer layer in CdTe heterojunction solar cells, particularly in structures such as p-CdTe/n-3C-SiC/n-SnO_2 using SCAPS-1D. they have examined the effects of defect density and environmental conditions on device performance and found that the optimizing buffer layer increase PCE from 10.1% to 17.29%. Table 2 shows a comparison between theoretical results of using 3C-SiC with different absorbing layers such as CIGS and CdTe and compare them with the current results.

4. Conclusions

This study demonstrates that the incorporation of a SiC interlayer strongly influences the optoelectronic performance of P3HT/ZnS hybrid solar cells. Among the polytypes, 3C-SiC provides the most favourable conduction- and valence-band alignment, resulting in efficient charge extraction, reduced interfacial recombination, and enhanced photovoltaic parameters. Using a 6H-SiC interlayer results in moderate performance improvement, while the 4H-SiC introduces energy barriers that increase recombination and series resistance, limiting device efficiency. In contrast, optimizing the 3C-SiC interlayer thickness in the range of 70-100 nm greatly improves band bending, widens the depletion region, and smooths the interfacial potential. These changes result in higher short-circuit current density (J_{SC}), fill factor (FF), and power conversion efficiency (PCE). Further analysis shows that device performance is strongly affected by trap density, effective density of states, and resistive losses. These results highlight the importance of choosing the right SiC polytype and carefully controlling interlayer thickness to improve charge transport and efficiency in hybrid solar cells. Among all configurations studied, 3C-SiC stands out as the most promising option for high-performance and stable hybrid photovoltaic devices. However, this study is based on simulations and does not include experimental validation. It also assumes ideal material properties and does not address long-term stability or fabrication challenges. Future work should include experimental verification, improved interface and defect control, and evaluation of stability and scalability for practical applications.

Acknowledgements

The authors would like to thank Alex Niemegeers, Marc Burgelman, Koen Decock, Stefaan Degrave, and Johan Verschraegen for their contributions to the development of the SCAPS-1D software. The authors also gratefully acknowledge Ghent University, Belgium, for providing this software free of charge and supporting ongoing research in solar cell technology.

Nomenclature

C	Capacitance	F
E_C	Conduction band energy	eV
E_F	Fermi level energy	eV
E_g	Band gap	eV
E_V	Valence band energy	eV
FF	Fill Factor	%
J_{max}	Current density at maximum point	$mA \cdot cm^{-2}$
J_{ph}	Photocurrent density	$mA \cdot cm^{-2}$
J_{SC}	Short-circuit current density	$mA \cdot cm^{-2}$
K_B	Boltzmann constant	$J \cdot K^{-1}$
N_A	Acceptor density	cm^{-3}
N_C	Conduction band density of states	cm^{-3}
N_D	Donor density	cm^{-3}
N_V	Valence band density of states	cm^{-3}
PCE	Power Conversion Efficiency	%
V_{OC}	Open-circuit voltage	V
V_{max}	Voltage at maximum point	V
W	Depletion width	mm
χ	Electron affinity	eV
ε	Dielectric constant	—
μ_e	Electron mobility	$m^2 \cdot V^{-1} \cdot s^{-1}$
μ_h	Hole mobility	$m^2 \cdot V^{-1} \cdot s^{-1}$
σ	Conductivity	$S \cdot m^{-1}$

References

[1] Feng, Z. C., Lin, H. H., Xin, B., Tsai, S. J., Saravade, V., Yiin, J., Klein, B., & Ferguson, I. T. (2023). Structural characteristics of 3C-SiC thin films grown on Si-face and C-face 4H-SiC substrates by high temperature chemical vapor deposition. Vacuum, 207, 111643. https://doi.org/10.1016/j.vacuum.2022.111643

[2] Bhatnagar, M., & Baliga, B. J. (1993). Comparison of 6H-SiC, 3C-SiC, and Si for power devices. IEEE Transactions on Electron Devices, 40(3), 645-655. https://doi.org/10.1109/16.199372

[3] Harris, C. I., Savage, S., Konstantinov, A., Bakowski, M., & Ericsson, P. (2001). Progress towards SiC products. Applied Surface Science, 184(1-4), 393-398. https://doi.org/10.1016/S0169-4332(01)00525-6

[4] Schöner, A., Krieger, M., Pensl, G., Abe, M., & Nagasawa, H. (2006). Fabrication and characterization of 3C-SiC-based MOSFETs. Chemical Vapor Deposition, 12(8-9), 523-530. https://doi.org/10.1002/cvde.200606467

[5] Ferry, D. K. (1975). High-field transport in wide-band-gap semiconductors. Physical Review B, 12(6), 2361. https://doi.org/10.1103/PhysRevB.12.2361

[6] Huang, J. J., Militzer, C., Wijayawardhana, C., Forsberg, U., Ojamae, L., & Pedersen, H. (2022). Controlled CVD growth of highly ⟨111⟩-oriented 3C-SiC. The Journal of Physical Chemistry C, 126(23), 9918-9925.https://doi.org/10.1021/acs.jpcc.2c01171

[7] Syväjärvi, M., Ma, Q., Jokubavicius, V., Galeckas, A., Sun, J., Liu, X., et al. (2016). Cubic silicon carbide as a potential photovoltaic material. Solar Energy Materials and Solar Cells, 145, 104-108. https://doi.org/10.1016/j.solmat.2015.08.029

[8] Yang, N., Zhuang, H., Hoffmann, R., Smirnov, W., Hees, J., Jiang, X., & Nebel, C. E. (2011). Nanocrystalline 3C-SiC electrode for biosensing applications. Analytical Chemistry, 83(15), 5827-5830. https://doi.org/10.1021/ac201315q

[9] Kato, M., Yasuda, T., Miyake, K., Ichimura, M., & Hatayama, T. (2014). Epitaxial p-type SiC as a self-driven photocathode for water splitting. International Journal of Hydrogen Energy, 39(10), 4845-4849. https://doi.org/10.1016/j.ijhydene.2014.01.049

[10] Yazdi, G. R., Iakimov, T., & Yakimova, R. (2016). Epitaxial graphene on SiC: A review of growth and characterization. Crystals, 6(5), 53. https://doi.org/10.3390/cryst6050053

[11] Yazdi, G. R., Vasiliauskas, R., Iakimov, T., Zakharov, A., Syväjärvi, M., & Yakimova, R. (2013). Growth of large area monolayer graphene on 3C-SiC and a comparison with other SiC polytypes. Carbon, 57, 477-484. https://doi.org/10.1016/j.carbon.2013.02.022

[12] Backes, C., Abdelkader, A. M., Alonso, C., et al. (2020). Production and processing of graphene and related materials. 2D Materials, 7(2), 022001. https://doi.org/10.1088/2053-1583/ab1e0a

[13] Shi, Y. (2019). Growth of 3C-SiC and graphene for solar water-splitting application. Linköping University Dissertation. https://doi.org/10.3384/diss.diva-159100

[14] Janz, S., Reber, S., Lutz, F., & Schetter, C. (2006). Conductive SiC as an intermediate layer for CSITF solar cells. Thin Solid Films, 511, 271-274. https://doi.org/10.1016/j.tsf.2005.11.102

[15] Sameera, J. N., Islam, M. A., Islam, S., Hossain, T., Sobayel, M. K., Akhtaruzzaman, M., et al. (2022). Cubic silicon carbide (3C-SiC) as a buffer layer for high efficiency CdTe solar cell. Optical Materials, 123, 111911. https://doi.org/10.1016/j.optmat.2021.111911
[16] Zouache, R., Saidani, O., Yousfi, A., Alsubaie, A. S., Soulef, B. A., Feriel, L., & Islam, R. (2025). Numerical investigation of enhanced efficiency in CIGS solar cells with 3C-SiC and PEDOT:PSS integration. Periodica Polytechnica Chemical Engineering, 69(1), 26-34. https://doi.org/10.3311/PPch.38770
[17] Wang, L., Yang, F., Pei, Y., Yang, X., & Lorenz, L. (2026). Packaging and integration of silicon carbide power devices. Nature Reviews Electrical Engineering. https://doi.org/10.1038/s44287-026-00263-0
[18] Hasan, A. A., Zuhdi, A. M., Al-Ghaili, A. M., Al-Shetwi, A. Q., Islam, M. A., Sankar, K. P., & Gunasekaran, S. S. (2025). A review on silicon photovoltaic module degradations and recent identification techniques. Solar Energy, 288, 113288. https://doi.org/10.1016/j.solener.2025.113288
[19] Kadem, B. Y., & Abbas, E. M. (2024). Optimization of several parameters towards 30% efficiency perovskite solar cell using SCAPS-1D software. Iraqi Journal of Physics, 22(4), 117-129.
[20] Yassine, B., Tahar, B., & Fathi, G. (2022). Modeling and simulation of CZTS based solar cells using SCAPS-1D. Chalcogenide Letters, 19(8), 503-511. https://doi.org/10.15251/CL.2022.198.503
[21] Mekaret, F., et al. (2024). A comparative study of Schottky barrier heights and charge transport mechanisms in SiC polytypes. AIP Advances, 14(11). https://doi.org/10.1063/5.0240123
[22] Kadem, B., Hassan, A., & Cranton, W. (2016). Efficient P3HT:PCBM solar cells. Journal of Materials Science: Materials in Electronics, 27(7), 7038-7048. https://doi.org/10.1007/s10854-016-4661-8
[23] Sofia, J. R., & Wilson, K. J. (2023). Optimization of Jsc in DSSCs. Optik, 290, 171287. https://doi.org/10.1016/j.ijleo.2023.171287
[24] Kadem, B. Y. (2025). PEDOT:PSS thin films for solar cells. Nanomaterials and Energy, 14(2), 1-10. https://doi.org/10.1680/jnaen.24.00014
[25] Brudnyi, V. N., & Kosobutsky, A. V. (2017). Electronic properties of SiC polytypes. Superlattices and Microstructures, 111, 499-505. https://doi.org/10.1016/j.spmi.2017.07.003
[26] Tress, W., et al. (2015). Radiative and non-radiative recombination in perovskites. Advanced Energy Materials, 5(3), 1400812. https://doi.org/10.1002/aenm.201400812
[27] Sozzi, G., et al. (2016). CIGS CV characteristics analysis. IEEE PVSC. https://doi.org/10.1109/PVSC.2016.7750043
[28] Zerfaoui, H., Dib, D., & Kadem, B. (2019). SiC solar cell light intensity effects. Silicon, 11(4), 1917-1923. https://doi.org/10.1007/s12633-018-0011-1
[29] McIntosh, K. R., et al. (2009). Luminescent down-shifting in Si solar cells. Progress in Photovoltaics, 17(3), 191-197. https://doi.org/10.1002/pip.867
[30] Jian, J., et al. (2019). NiO/3C-SiC photoanode. Journal of Materials Chemistry A, 7(9), 4721-4728. https://doi.org/10.1039/C9TA00020H
[31] Morab, S., Sundaram, M. M., & Pivrikas, A. (2023). Review on charge carrier transport in inorganic and organic semiconductors. Coatings, 13(9), 1657. https://doi.org/10.3390/coatings13091657
[32] Al-Hashimi, M. K., Kadem, B. Y., & Hassan, A. K. (2018). Rutile TiO_2 films as electron transport layer in inverted organic solar cell. Journal of Materials Science: Materials in Electronics, 29(9), 7152-7160. https://doi.org/10.1007/s10854-018-8703-2
[33] Liu, X., Guo, J., Hao, R., Zhao, Q., Chang, F., Wang, L., Liu, B., Li, Y., & Gu, K. (2019). Cliff-like conduction band offset at $CdS/Cu_2 ZnSnS_4$ heterojunction prepared by sputtering CuSn alloy target. Solar Energy, 183, 285-292. https://doi.org/10.1016/j.solener.2019.03.033
[34] Wang, A., He, M., Green, M. A., Sun, K., & Hao, X. (2023). A critical review on the progress of kesterite solar cells. Advanced Energy Materials, 13(2), 2203046. https://doi.org/10.1002/aenm.202203046
[35] Baig, F., Khattak, Y. H., Shuja, A., Riaz, K., & Soucase, B. M. (2020). Performance investigation of $Sb_2 Se_3$ solar cells in SCAPS-1D. Current Applied Physics, 20(8), 973-981. https://doi.org/10.1016/j.cap.2020.06.005
[36] Ghorbani, E. (2020). On efficiency of earth-abundant chalcogenide photovoltaic materials. Journal of Physics: Energy, 2(2), 025002. https://doi.org/10.1088/2515-7655/ab6942
[37] Vollbrecht, J., Tokmoldin, N., Sun, B., et al. (2023). Effective mobility in organic solar cells. Energy Advances, 2(9), 1390-1398. https://doi.org/10.1039/D3YA00125C
[38] Kasap, S. O. (2006). Electronic materials and devices (pp. 336-339). McGraw-Hill.
[39] Betti, M. G., Corradini, V., Bertoni, G., Casarini, P., Mariani, C., & Abramo, A. (2001). Density of

states of a two-dimensional electron gas. Physical Review B, 63(15), 155315. https://doi.org/10.1103/PhysRevB.63.155315
[40] Xia, J., Sohail, M., & Nazeeruddin, M. K. (2023). Interface engineering in perovskite solar cells. Advanced Materials, 35(31), 2211324. https://doi.org/10.1002/adma.202211324
[41] Davydov, S. Y. (2007). Electron affinity of silicon carbide polytypes. Semiconductors, 41(6), 696-698.
https://doi.org/10.1134/S1063782607060152
[42] Kephart, J. M., McCamy, J. W., Ma, Z., et al. (2016). Band alignment in CdTe solar cells. Solar Energy Materials and Solar Cells, 157, 266-275. https://doi.org/10.1016/j.solmat.2016.05.050
[43] Yang, Q., Bittkau, K., Eberst, A., Rau, U., & Ding, K. (2024). Interface recombination in silicon solar cells. Solar Energy Materials and Solar Cells, 273, 112953. https://doi.org/10.1016/j.solmat.2024.112953
[44] Haq, A. U., Buerkle, M., Askari, S., et al. (2020). Energy-level alignment in silicon carbide nanocrystals. The Journal of Physical Chemistry Letters, 11(5), 1721-1728. https://doi.org/10.1021/acs.jpclett.9b03828
[45] Bagade, S. S., Barik, S. B., Malik, M. M., & Patel, P. K. (2023). Band alignment in perovskite solar cells. Materials Today: Proceedings. https://doi.org/10.1016/j.matpr.2023.02.117
[46] Lopez-Varo, P., Jiménez-Tejada, J. A., García-Rosell, M., et al. (2018). Device physics of hybrid perovskite solar cells. Advanced Energy Materials, 8(14), 1702772. https://doi.org/10.1002/aenm.201702772
[47] Ahmed, A., Riaz, K., Mehmood, H., et al. (2020). ETL optimization in perovskite solar cells. Optical Materials, 105, 109897. https://doi.org/10.1016/j.optmat.2020.109897
[48] Ding, C., Zhang, Y., Liu, F., et al. (2018). Conduction band offset in perovskite solar cells. Nano Energy, 53, 17-26. https://doi.org/10.1016/j.nanoen.2018.08.031
[49] Bivour, M., Schröer, S., & Hermle, M. (2013). TCO/a-Si:H contact properties. Energy Procedia, 38, 658-669.
https://doi.org/10.1016/j.egypro.2013.07.330
[50] Kesavan, A. V., Rao, A. D., & Ramamurthy, P. C. (2017). Interface morphology in organic photovoltaics. ACS Applied Materials & Interfaces, 9(34), 28774-28784. https://doi.org/10.1021/acsami.7b03953
[51] Armstrong, C. L., Price, M. B., Munoz-Rojas, D., et al. (2015). Inorganic interlayers in hybrid solar cells. ACS Nano, 9(12), 11863-11871. https://doi.org/10.1021/acsnano.5b05934
[52] Kim, H., Lee, K. S., Paik, M. J., et al. (2022). PMMA interlayer in perovskite solar cells. Advanced Functional Materials, 32(13), 2110473. https://doi.org/10.1002/adfm.202110473
[53] Sherkar, T. S., Momblona, C., Gil-Escrig, L., et al. (2017). Recombination in perovskite solar cells. ACS Energy Letters, 2(5), 1214-1222. https://doi.org/10.1021/acsenergylett.7b00236
[54] Singh, P., & Ravindra, N. M. (2012). Temperature dependence of solar cell performance. Solar Energy Materials and Solar Cells, 101, 36-45. https://doi.org/10.1016/j.solmat.2012.02.019
[55] Shaker, L. M., Al-Amiery, A. A., Hanoon, M. M., et al. (2024). Thermal effects on solar cells. Sustainable Energy Research, 11(1), 6. https://doi.org/10.1186/s40807-024-00100-8
[56] Mundhaas, N., Yu, Z. J., Bush, K. A., et al. (2019). Series resistance in perovskite solar cells. Solar RRL, 3(4), 1800378. https://doi.org/10.1002/solr.201800378
[57] Park, Y., Noh, S., Lee, D., Kim, J. Y., & Lee, C. (2011). Temperature dependence in polymer solar cells. Journal of the Korean Physical Society, 59(2), 362-366. https://doi.org/10.3938/jkps.59.362
[58] Scheunemann, D., Wilken, S., Parisi, J., & Borchert, H. (2016). Charge carrier loss in $CuInS_2$ /ZnO solar cells. Physical Chemistry Chemical Physics, 18(24), 16258-16265. https://doi.org/10.1039/C6CP01015F
[59] Kumar, A., & Ranjan, P. (2021). VOC characterization in thin-film solar cells. Solar Energy, 220, 35-42. https://doi.org/10.1016/j.solener.2021.03.017
[60] Sobayel, M. K., Chowdhury, M. S., Hossain, T., et al. (2021). Efficiency enhancement of CIGS solar cells using 3C-SiC buffer layer. Solar Energy, 224, 271-278.
https://doi.org/10.1016/j.solener.2021.05.093